OPEN ACCESS



CECILIA: The Faint Emission Line Spectrum of $z \sim 2-3$ Star-forming Galaxies

Allison L. Strom^{1,2}, Gwen C. Rudie³, Ryan F. Trainor⁴, Gabriel B. Brammer⁵, Michael V. Maseda⁶, Menelaos Raptis⁴, Noah S. J. Rogers^{1,2,7}, Charles C. Steidel⁸, Yuguang Chen (陈昱光)⁹, and David R. Law¹⁰ Department of Physics and Astronomy, Northwestern University, 2145 Sheridan Road, Evanston, IL 60208, USA; allison.strom@northwestern.edu² Center for Interdisciplinary Exploration and Research in Astrophysics (CIERA), Northwestern University, 1800 Sherman Avenue, Evanston, IL 60201, USA

3 Carnegie Observatories, 813 Santa Barbara Street, Pasadena, CA 91101, USA

4 Department of Physics and Astronomy, Franklin & Marshall College, 637 College Avenue, Lancaster, PA 17603, USA

5 Cosmic Dawn Center (DAWN), Niels Bohr Institute, University of Copenhagen, Jagtvej 128, København N, DK-2200, Denmark

6 Department of Astronomy, University of Wisconsin, 475 N. Charter Street, Madison, WI 53706, USA

7 Minnesota Institute for Astrophysics, University of Minnesota, 116 Church St. SE, Minneapolis, MN 55455, USA

8 Cahill Center for Astronomy and Astrophysics, California Institute of Technology, MS 249-17, Pasadena, CA 91125, USA

9 Department of Physics and Astronomy, University of California, Davis, 1 Shields Avenue, Davis, CA 95616, USA

10 Space Telescope Science Institute, 3700 San Martin Drive, Baltimore, MD 21218, USA

Received 2023 August 24; revised 2023 October 23; accepted 2023 October 24; published 2023 November 20

Abstract

We present the first results from Chemical Evolution Constrained Using Ionized Lines in Interstellar Aurorae (CECILIA), a Cycle 1 JWST NIRSpec/MSA program that uses ultra-deep \sim 30 hr G235M/F170LP observations to target multiple electron temperature-sensitive auroral lines in the spectra of 33 galaxies at $z\sim$ 1–3. Using a subset of 23 galaxies, we construct two \sim 600 object-hour composite spectra, both with and without the stellar continuum, and use these to investigate the characteristic rest-optical ($\lambda_{\rm rest}\approx$ 5700–8500 Å) spectrum of star-forming galaxies at the peak epoch of cosmic star formation. Emission lines of eight different elements (H, He, N, O, Si, S, Ar, and Ni) are detected, with most of these features observed to be \lesssim 3% the strength of H α . We report the characteristic strength of three auroral features ([N II] λ 5756, [S III] λ 6313, and [O II] $\lambda\lambda$ 7322, 7332), as well as other semi-strong and faint emission lines, including forbidden [Ni II] $\lambda\lambda$ 7380, 7414 and permitted O I λ 8449, some of which have never before been observed outside of the local Universe. Using these measurements, we find T_e [N II] = 13,630 \pm 2540 K, representing the first measurement of electron temperature using [N II] in the high-redshift Universe. We also see evidence for broad line emission with a FWHM of 536 $^{+45}_{-167}$ km s $^{-1}$; the broad component of H α is 6.01%–28.31% the strength of the narrow component and likely arises from star-formation-driven outflows. Finally, we briefly comment on the feasibility of obtaining large samples of faint emission lines using JWST in the future.

Unified Astronomy Thesaurus concepts: High-redshift galaxies (734); Emission line galaxies (459); Galaxy spectroscopy (2171); Chemical abundances (224)

1. Introduction

The nebular emission lines originating in galaxies' starforming regions are among the most powerful tools available for investigating the physical conditions in galaxies at all redshifts (see Kewley et al. 2019 for a review). Recombination lines of hydrogen provide constraints on star formation rates (SFRs) and reddening due to dust; weaker recombination lines of heavier elements such as oxygen are direct tracers of gasphase enrichment; and collisionally excited forbidden transitions of elements like oxygen, nitrogen, carbon, and sulfur are variously sensitive to electron temperature (T_e) and electron density (n_e), as well as the ionization state and enrichment of the photoionized gas.

Some of these lines, including H α at 6564 Å and the [O III] $\lambda\lambda$ 4960, 5008 doublet, are bright enough to be detected out to large cosmological distances, even with relatively short exposure times. Indeed, over the last decade, ground-based near-infrared (NIR) spectrographs such as Magellan/FIRE (Simcoe et al. 2008, 2010), Keck/MOSFIRE (McLean et al. 2010, 2012), and the Very Large Telescope (VLT)/

Original content from this work may be used under the terms of the Creative Commons Attribution 4.0 licence. Any further distribution of this work must maintain attribution to the author(s) and the title of the work, journal citation and DOI.

KMOS (Sharples et al. 2013) have led to samples of thousands of $z \sim 2-3$ galaxies with measurements of such emission lines (e.g., Masters et al. 2014; Steidel et al. 2014; Sanders et al. 2015; Shapley et al. 2015; Wisnioski et al. 2015; Strom et al. 2017), allowing their metallicity, ionization and excitation properties, and gas density to be studied in comparable detail to large samples of $z \sim 0$ galaxies (e.g., Kauffmann et al. 2003; Brinchmann et al. 2004; Tremonti et al. 2004; Belfiore et al. 2015; Mingozzi et al. 2020). In the last year, JWST/NIRSpec and JWST/NIRCam grism observations have extended these efforts to even higher redshifts ($z \gtrsim 3-6$) by enabling infrared (IR) spectroscopy out to longer wavelengths (e.g., Kashino et al. 2023; Kocevski et al. 2023; Oesch et al. 2023; Shapley et al. 2023; Sun et al. 2023).

Other lines—including metal recombination lines and the T_e -sensitive auroral lines of heavy elements, which are both key probes of chemical enrichment—are faint enough that they are not routinely detected even in spectra of nearby galaxies. Despite significant investment of observing time on some of the largest ground-based telescopes in the world, measurements of auroral $[O III]\lambda 4364$ were only possible for a handful of individual galaxies at $z \gtrsim 2$ prior to the launch of JWST (Christensen et al. 2012; James et al. 2014; Sanders et al. 2020). Spectroscopic observations with JWST promise to yield unprecedented numbers of auroral emission line measurements in high-z

galaxies. The first analyses of the early release observations (EROs; Pontoppidan et al. 2022) in the SMACS J0723.37327 field reinforced this expectation, with significant detections of [O III] λ 4364 in several $z \sim 8$ galaxies (Arellano-Córdova et al. 2022; Schaerer et al. 2022; Taylor et al. 2022; Brinchmann 2023; Curti et al. 2023; Katz et al. 2023; Rhoads et al. 2023; Trump et al. 2023; Trussler et al. 2023). At the same time, many of these studies reported conflicting gas-phase oxygen abundance (O/H) measurements in the same objects, and it was unclear how representative this early, very-high-z sample might be. Subsequent work has revisited the issue of auroral line detections in JWST observations of tens of high-z galaxies (albeit primarily at low to moderate O/H), confirming suspicions that locally calibrated metallicity diagnostics are likely unsuitable for the majority of high-z galaxies (Sanders et al. 2023a; Laseter et al. 2023). To date, however, consensus regarding how best to leverage these measurements to understand the overall distribution of chemical enrichment in the early Universe has not yet been achieved.

In spite of these challenges, the community has collectively recognized the goal of using auroral line measurements and the resulting direct-method metallicities to construct more accurate methods of measuring high-z galaxy enrichment in situ. This is evidenced by the selection of three separate Cycle 1 JWST programs (PIDs 1879, 1914, and 2593) by the time-allocation committee, with a total investment of over 150 hr, or $\sim 2.5\%$ of all the GO time available in Cycle 1. Here, we report the first results from PID 2593, also known as Chemical Evolution Constrained Using Ionized Lines in Interstellar Aurorae (CECILIA; Strom et al. 2021).

CECILIA was designed to measure auroral [S III] λ 6313 and [O II] $\lambda\lambda$ 7322, 7332 in the spectra of a carefully selected sample of $z\sim2-3$ star-forming galaxies, using \sim 30 hr G235M/F170LP observations. Owing to the unique depth of these data, CECILIA is also able to detect myriad other lines in the galaxies' rest-optical spectra, some of which are stronger than any auroral emission line and, thus, more likely to be observed in more typical integration times with JWST. Consequently, it is important to understand the expected strengths of these faint and semi-strong emission lines in order to guide future studies using JWST, as well as with other current and future facilities.

The remainder of this Letter focuses on two \sim 600 object-hour rest-optical composite spectra of $z\sim2-3$ galaxies observed as part of the CECILIA survey, with the aim of providing an "atlas" of the characteristic faint emission line spectrum of high-z galaxies. We describe the CECILIA survey—including the galaxy sample, the JWST program, and the data reduction—in Section 2. Section 3 outlines the construction of the composite spectra and their key features, with a more in-depth discussion of individual emission lines in Section 4. In Section 5, we close with a summary of our findings and a brief discussion of implications for future observations of faint emission lines in $z\gtrsim2$ galaxies. Throughout the text, we refer to specific spectral features using their vacuum wavelengths.

2. The CECILIA Survey

The principal goal of CECILIA is to measure multiple faint rest-optical auroral lines in the spectra of $z \sim 2-3$ galaxies, which can then be used to calibrate new high-z metallicity diagnostics. Some of the galaxies observed as part of CECILIA have preexisting rest-optical spectra obtained using Keck/

MOSFIRE (Steidel et al. 2014; Trainor et al. 2015; Strom et al. 2017), but even the strongest auroral lines are not routinely detected for individual galaxies in deep (\sim 8–10 hr) observations. Although JWST/NIRSpec provides greater sensitivity and spectral coverage than ground-based NIR spectrographs, achieving this goal still pushes the limits of the observatory. To make the best use of JWST observing time, we first used detailed photoionization models and existing ground-based rest-ultraviolet (UV) and rest-optical spectra of the same galaxies to robustly predict the auroral line strengths. We then used these predictions together with the (preflight) JWST Exposure Time Calculator (ETC)¹¹ to identify the depth needed to detect the auroral lines in individual galaxies. Below, we describe the parent galaxy sample, the emission line predictions, the design of the NIRSpec program, including exposure-time requirements and microshutter assembly (MSA) design, and the reduction of the JWST data.

2.1. Parent Galaxy Sample and Field Selection

CECILIA targets galaxies drawn from the Keck Baryonic Structure Survey (KBSS; Steidel et al. 2010; Rudie et al. 2012; Trainor et al. 2015; Strom et al. 2017). KBSS is a large spectroscopic survey of UV-color and narrowband Lyaselected galaxies in 15 fields. The survey includes deep J, H, and K NIR (rest-optical) spectroscopy from Keck/MOSFIRE, deep optical (rest-UV) spectroscopy from Keck/LRIS, and imaging in U_n through K_s , Hubble Space Telescope (HST)/ WFC3 F140W and F160W, Spitzer IRAC Chs 1-4 and MIPS 24 μ m, and narrowband (rest-frame) Ly α filters. In total, KBSS comprises $\sim 3500 z \sim 1-3$ galaxies with confirmed (rest-UV or rest-optical) spectroscopic redshifts and rich multiwavelength data. Thanks to the dense sampling of galaxies with known redshifts and high-quality rest-optical spectroscopy in KBSS, targeting one of the survey fields allows us to efficiently prioritize those galaxies predicted to yield auroral line detections, where we can also ensure that all of the emission lines required to determine T_e and direct-method metallicity are accessible.

The primary targets for CECILIA are UV-color-selected galaxies for which detecting the auroral [S III] λ 6313 line is feasible, as this is the faintest line required to achieve the primary goals of the program (see Section 2.2). We focused on galaxies with $2.10 \le z \le 2.68$, where all of the required emission lines fall within the G235M, G395M, and groundbased NIR spectral bandpasses. Galaxies were prioritized if they have somewhat higher redshifts (z > 2.3), where NIRSpec is more sensitive at the observed wavelength of [S III] λ 6313; smaller than average sizes, increasing the auroral surface brightness; high spectral energy distribution (SED)based SFRs (>24 M_{\odot} yr⁻¹); and/or large observed nebular [O III] $\lambda 5008$ or H α line fluxes (>7.0 × 10⁻¹⁷ erg s⁻¹ cm⁻²). All of these properties increase the ease of detection with the NIRSpec/MSA. The highest-priority targets were galaxies with detailed emission line models (Section 2.2) whose predicted auroral line surface brightnesses exceeded the detection threshold of the planned observations; galaxies with models predicting nondetections were down-weighted. Narrowbandselected Ly α emitters (LAEs) from Trainor et al. (2016) with spectroscopic detections of Ly α and [O III] λ 5008 or H α were

¹¹ https://jwst.etc.stsci.edu/

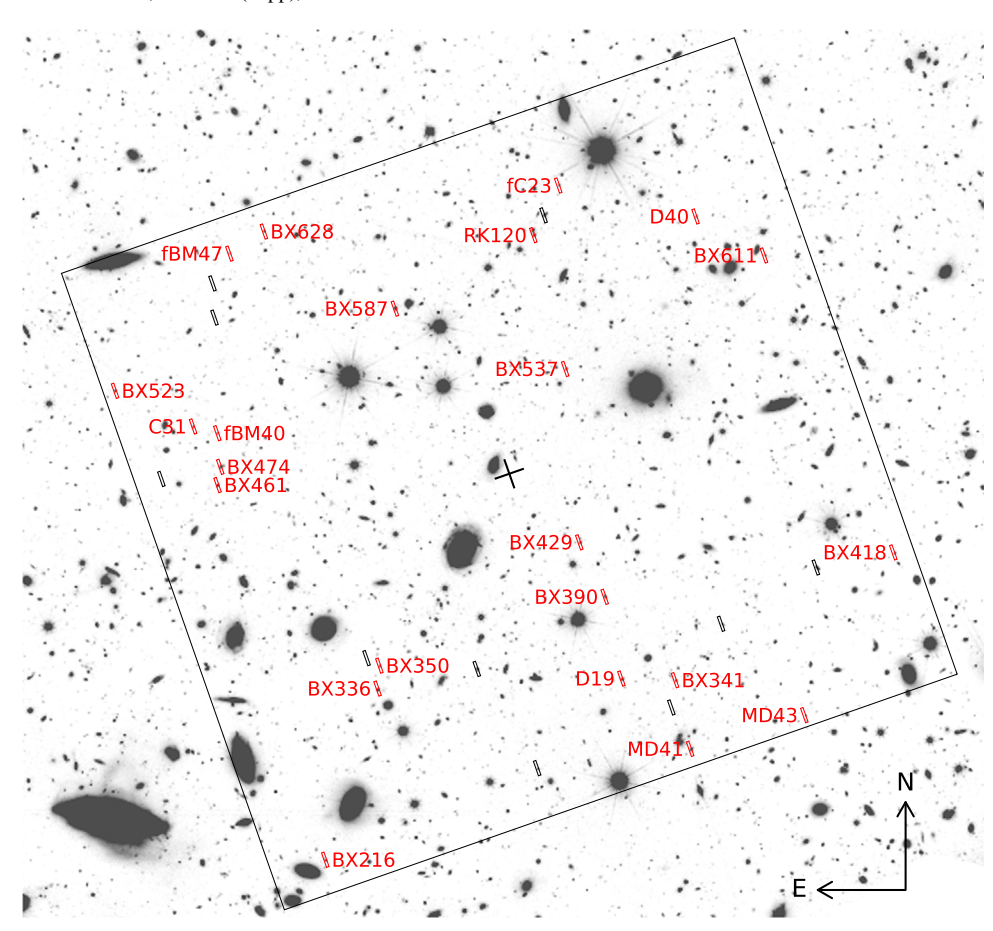


Figure 1. The HST/WFC3 F140W image of the Q2343+125 field targeted by CECILIA is shown in grayscale, with the approximate $3'.6 \times 3'.4$ NIRSpec field of view overlaid in black. The observed slits are magnified by $\sim 3 \times$ for visibility, with red slits and names indicating the 23 sources included in this work.

also prioritized as a way of extending the galaxy sample to lower stellar masses (M_*) and SFRs.

Of the 15 KBSS fields, we selected the Q2343+125 field due to its high density of high-priority sources and large catalog of LAEs at $z\approx 2.55$ with spectroscopic redshifts. Further, this field also has an existing HST/WFC3 F140W mosaic (Figure 1) that provided both the precision astrometry required for mask design and the galaxy size measurements needed for target prioritization—without requiring additional (pre)imaging from space using JWST or HST.

The CECILIA JWST/NIRSpec observations contain a total sample of 34 galaxies. ¹² We include 23 of these objects here (Figure 1), omitting the Ly α -selected galaxies that do not have secure SED models (four galaxies), galaxies at z < 2 (four galaxies), and sources that were severely impacted by shutter failures in the NIRSpec/MSA (three galaxies). The final sample is largely typical of KBSS galaxies, with $\langle z \rangle = 2.4$, masses spanning $\log(M_*/M_\odot) = 8.5-10.7$, and a median value of $\log(M_*/M_\odot) = 9.7$ (assuming a Chabrier 2003 stellar initial mass function). Based on $H\alpha$ and $H\beta$ measurements from ancillary MOSFIRE spectra, the included galaxies have SFRs ranging from 16 to $42~M_\odot$ yr⁻¹, with a median SFR_{H α} = $21~M_\odot$ yr⁻¹. These are slightly lower than the median values reported in Strom et al. (2017), which were determined in the same manner, but are similar in terms of M_* to the subsample of

KBSS galaxies used to construct the deep "LM1" composite in Steidel et al. (2016).

2.2. Emission Line Predictions

The expected strengths of the auroral emission lines targeted by CECILIA were determined using photoionization models designed to reconcile the rest-UV and rest-optical spectra of $z\sim 2-3$ galaxies. We used a combination of the Binary Population and Spectral Synthesis models (BPASSv2; Stanway et al. 2016; Eldridge et al. 2017) and Cloudy photoionization models (Cloudy13; Ferland et al. 2013) to predict line strengths as a function of gas-phase metallicity (O/H). We matched the model parameters (gas density $n_{\rm H}$, stellar Fe/H, and ionization parameter U) to the properties of $z\sim 2-3$ KBSS galaxies reported by Strom et al. (2018), which are consistent with the values reported for other $z\sim 2-3$ samples (e.g., Topping et al. 2020). The model outputs were then converted to line fluxes using a representative range of SFRs and dust extinction.

Figure 2 presents the predictions for three of the brightest rest-optical auroral emission lines as a function of O/H, with the width of the hatched regions corresponding to the typical range of U in high-z galaxies; lower-ionization galaxies have fainter lines at fixed metallicity. Recalibrating strong line metallicity diagnostics and photoionization models at $z \gtrsim 2$ requires measuring auroral lines in galaxies spanning both O/H and U, as both directly influence the strength of nebular emission lines. The top panel in Figure 2 shows the steep decline in $[O III]\lambda 4364$ with increasing O/H and implies a limited ability to detect typical $z \sim 2$ galaxies

 $[\]overline{^{12}}$ One target, Q2343-D27, appears to be a z = 0.0890 interloper, based on the JWST/NIRSpec observations.

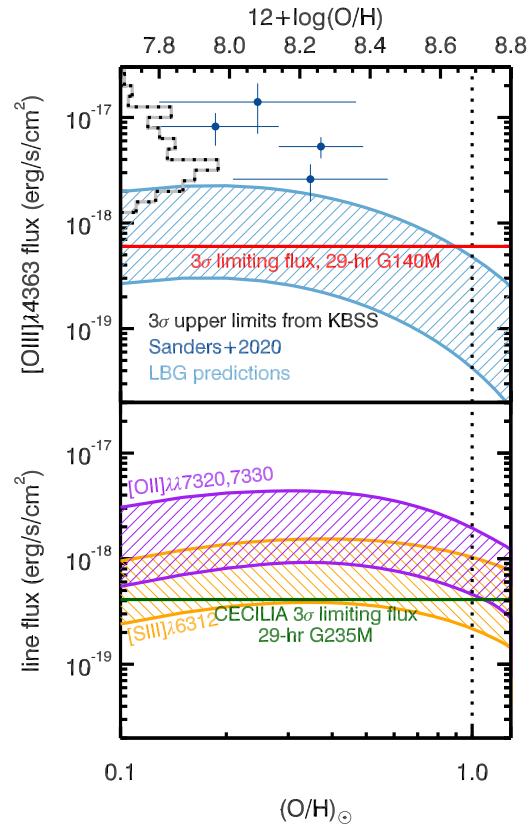


Figure 2. The hatched regions show the model predictions for auroral lines in the rest-optical spectra of typical $z \sim 2-3$ galaxies, separated on the basis of whether they fall in the G140M bandpass (top panel) or the G235M bandpass (bottom panel). The width of the hatched regions reflects the typical range of the ionization parameter U in high-z galaxies. The predicted line fluxes for [O III] λ 4364 (blue hatched region) are \sim 1 dex fainter than the depth of typical ground-based spectra of individual galaxies, represented by the distribution of 3σ upper limits on [O III] λ 4364 from KBSS (dashed black histogram). Sanders et al. (2020) reported four ground-based detections of unlensed [O III] λ 4364 (blue points, shifted up by 0.24 dex to match the photoionization model abundance scale), but these galaxies appear atypical. Estimates using the preflight ETC indicated that detecting $[O~III]\lambda 4364$ in a representative sample of high-z galaxies would be prohibitively expensive; the 3σ limiting line flux of 6×10^{-19} erg s⁻¹ cm⁻² achievable in a combined 29 br G140M exposure (red erg s⁻¹ cm⁻² achievable in a combined 29 hr G140M exposure (red line) probes $\lesssim 30\%$ of the $z \sim 2-3$ sample from Strom et al. (2018). Fortunately, the typical predicted line fluxes for the sum of the [O II] $\lambda\lambda7322$, 7332 lines (purple hatched region) and [S III] $\lambda6313$ (orange hatched region) could be detected for galaxies with a wider range of U and O/H in the same exposure time, due to the higher sensitivity of NIRSpec in G235M. A 3σ limiting line flux of 4.1×10^{-19} erg s⁻¹ cm⁻² reaches $\sim 90\%$ of typical

at high O/H and/or low U using JWST/NIRSpec, even with long exposures in G140M.

In contrast, the bottom panel of Figure 2 shows that a 3σ line-flux sensitivity of 4.1×10^{-19} erg s⁻¹ cm⁻² in G235M (corresponding to a total ≈ 30 hr exposure time using the preflight ETC; see Section 2.3.1) enables the detection of [S III] $\lambda 6313$ and [O II] $\lambda \lambda 7322$, 7332 at virtually all U, even in galaxies with relatively high gas-phase O/H. It is comparatively easier to detect [S III] $\lambda 6313$ and [O II] $\lambda \lambda 7322$, 7332 not only because they are predicted to be intrinsically brighter than [O III] $\lambda 4364$ in the same galaxies, but also because of the increasing sensitivity of JWST/NIRSpec at longer wavelengths. On the basis of these predictions, we elected to obtain deep spectra of galaxies in a *single* configuration, in order to maximize the overall number of auroral lines detected for individual galaxies with a range of O/H and U.

2.3. JWST/NIRSpec Program Design

To optimize the efficiency of the JWST program, we generated a large grid of ETC simulations spanning a range of galaxy sizes, limiting line fluxes, MSA centering constraints, and redshifts, as well as a comparable grid of MSA Planning Tool (MPT) simulations that considered the full range of available centering constraints. In this section, we describe the most salient elements of the program design.

2.3.1. Exposure-time Requirements

NIRSpec G235M observations of [S III] λ 6313 and [O II] $\lambda\lambda$ 7322, 7332 in CECILIA galaxies were modeled using an exponential surface-brightness profile (Sérsic index n=1) with a projected semimajor axis of 0."26 and an axis ratio of b/a=0.6, consistent with the measured morphologies and median sizes of galaxies in our parent sample (Law et al. 2012).

Preflight ETC simulations showed that reaching the required 3σ limiting line flux of 4.1×10^{-19} erg s⁻¹ cm⁻² for a mediansized galaxy at z = 2.3 at the edge of the midpoint tolerance (see Section 2.3.2) required 29.5 hr of exposure time (20 groups \times six integrations \times 12 exposures) using NRS IRS2 readouts. Our exposure-time calculations assumed "MSA Full Shutter Extraction" and assumed we would need pixel-level subtraction from A-B pairs. As we discuss below, in Section 2.4.1, we have instead implemented a global background model drawn from slits across the full MSA, which reduces the overall noise in the final combined data compared to the conservative assumptions in our original calculations. For the majority of the sources in our catalog, ETC calculations demonstrated that some of the background region in each spectrum would be contaminated with light from the source, and the derived exposure-time requirements took this effect into account.

2.3.2. MSA Design

The MSA configuration is central to the success of CECILIA, and considerable experience with ground-based multi-object mask design led us to conduct extensive trials using different mask parameters in the MPT. We experimented with all possible centering constraints, dithering and nodding options, and three-and five-slitlet length slits. We ran trial masks spanning the full range of allowable position angles (PAs), using small steps in both position and PA to understand the sensitivity of the optimal configuration to changes in PA. Based on more than 100 runs of the MPT considering more than 70 million unique configurations, we determined that many PAs have <60% as many high-priority targets as the best masks.

We optimized the MSA centering constraint, which trades exposure time against sample size, by considering a grid of ETC and MPT runs. Our ETC calculations spanned the full redshift range of source galaxies and sizes ranging between the 1st and 3rd quartile of the KBSS size distribution. We considered the signal-to-noise ratio (S/N) penalty for galaxies at maximal offset in the dispersion direction for each of the three possible centering restrictions. ¹³ For galaxies with the median size in our sample, the S/N penalties compared to a perfectly centered target are 7%–13% for "constrained," 11%

¹³ The assumed offsets in the ETC are 0."063 for "constrained," 0."076 for "midpoint," and 0."099 for "entire open shutter." These values use the specified margin and the pitch of the MSA shutters, thus accounting for the current uncertainty in the width of the MSA bars.

-19% for "midpoint," and 14%-26% for "entire open shutter," where the reported ranges represent different relative angles between the short axis of the slit and the major axis of the galaxies. MPT runs showed that "constrained" configurations allowed for only 60% of the high-priority targets to be placed on a mask compared to the "midpoint" criteria. Relaxing the centering further via "entire open shutter" constraint only increased the number of high-priority targets by 7%. Therefore, we selected the "midpoint" centering constraint for CECILIA observations.

We designed custom software that processed the MPT MSA configurations to check the wavelength coverage 14 (using MSAViz 15) and confirmed that primary targets assigned to a slit on the MSA would have spectral coverage of the required auroral and nebular lines. This software also considers the known emission line properties, M_* , and SFRs of target galaxies, which we used to select a final mask configuration that appropriately sampled the parent sample to enable an effective metallicity calibration. We selected a default three-shutter slitlet shape with a three-point nod pattern within the slitlet.

Upon scheduling, we were assigned an aperture position angle, APA = 20.0, with values from 18.5 < APA < 20.0 able to be accommodated within the scheduling window. At this point, we completed a second set of MPT simulations, including PA steps of 0.1° and 0."025-0."01 position steps to optimize the PA and final mask. We did not reach convergence, ¹⁶ even with angle and position steps much finer than suggested by JDox, suggesting that significant computational resources would be required to fully optimize NIRSpec/ MSA observations. Based on our simulations, we ultimately selected an APA = 19.3. Over the 1.5° range allowable within the plan window, the MPT resulted in more than a 30% variation in the number of high-priority targets, and we advocate for conducting similar PA optimization to maximize the efficiency of other NIRSpec/MSA programs with low to moderate density of high-priority targets.

Following the selection of pointing and PA, we ran MPT with an expanded catalog to (i) check for contamination in any of the shutters known to be stuck open as of 2022 June and (ii) open shutters on dark regions of the sky to sample the background light across the field. These sky slitlets are described in our modeling of the global sky background in Section 2.4.1. Once the automated MSA configuration was determined by MPT, the solution was hand-edited using the MSA configuration editor to (i) elongate slits for high-priority targets where possible, (ii) add more background shutters close to high-priority targets to better sample relevant wavelength or field-position changes in the background, and (iii) add highpriority targets that did not meet our centering constraints but could be placed on a mask without conflicting with other highpriority targets. The final MSA design included 34 sources, 23 of which are included in the stacked spectra presented in this letter.

2.4. JWST/NIRSpec Data Reduction

The uncalibrated raw G235M data (uncal) frames were processed using the <code>jwst_level1</code> pipeline in the <code>grizli¹⁷</code> package version 1.8.9 from Brammer (2023). The level 1 pipeline in <code>grizli</code> uses the <code>calwebb</code> Science Calibration Pipeline (v1.10.0, CRDS_CONTEXT = <code>jwst_1100.pmap</code>; Bushouse et al. 2023) for the <code>group_scale</code> correction, initial flagging of bad pixels and saturated pixels, bias subtraction (including corrections to the bias using reference pixels), as well as corrections for detector linearity and persistence and subtraction of the dark current. Following these <code>calwebb</code> steps, clusters of pixels affected by snowball cosmic ray events were flagged and the ramp fit was calculated, including additional processing to detect and remove the effects of cosmic rays and detector defects. Finally, a gain correction was applied, resulting in the level 1 processed <code>rate</code> files.

Next, the level 1 processed files were corrected for correlated read noise, which manifests as vertical banding in the rate files. This 1/f noise, driven by small temperature variations in the ASIC readout electronics, was modeled and removed using the NSClean algorithm from Rauscher (2023). NSClean requires the user to create a mask that identifies areas on each of the two NIRSpec detectors that are unilluminated by source light; these areas are thus relatively clean tracers of the correlated readout noise. We tested many different mask design strategies in order to remove as much of the large-scale vertical banding as possible while also limiting the introduction of additional high-frequency noise, which we found to be a side effect of the NSClean algorithm in many cases. We determined the most effective masks for our program omitted entire rows of pixels in the rectified full-detector image if any portion of that row was illuminated. Mask designs that omitted only the limited range of pixels that were illuminated in a given row resulted in higher levels of high-frequency noise being introduced in the regions of the detectors that were illuminated by source light.

Following the 1/f noise correction by NSClean, we applied the preprocessing routine steps from \mathtt{msaexp}^{18} v0.6.11 from Brammer (2022), aside from the 1/f noise correction. This routine repeated the search for snowballs and additional detector defects, which were also masked. We applied a bias offset correction calculated from the median of unilluminated pixels in each frame and rescaled the read-noise array associated with each exposure so that it reflected the distribution of the same unilluminated pixels.

Next, we used msaexp to call the calwebb_spec2 JWST Science Calibration Pipeline (v1.10.0; Bushouse et al. 2023), which computed the World Coordinate System reference frame for the data (including the wavelength calibration), extracted the individual 2D spectra for each slit, and flat-fielded each 2D spectral cutout. Each spectral cutout was corrected for path loss, assuming the sources uniformly illuminate the slit (i.e., using the PATHLOSS_UN correction). Note that the current calwebb_spec2 pipeline does not apply path-loss corrections for slits more than three shutters in length, of which there are many in CECILIA, for reasons described in Section 2.3.2. Thus, we modified the pipeline to apply the uniform source path-loss correction to all slits. The pipeline correction for the bar shadows produced by the discretized MSA slitlets was then

 $[\]overline{^{14}}$ The postflight version of MPT now has the ability to output the wavelength coverage of individual slitlets.

https://github.com/spacetelescope/msaviz

¹⁶ We define a converged mask as one where the same optimal mask is returned even when the step size is decreased.

https://github.com/gbrammer/grizli

¹⁸ https://github.com/gbrammer/msaexp

applied to the data, although, as described in Section 2.4.1, the pipeline correction left residual bar shadows on the data and background illumination. The <code>calwebb_spec2</code> photom step then provided a final correction to the photometric calibration of the data, resulting in flux-calibrated 2D spectra for each slit and exposure. Finally, we used the <code>msaexpdrizzle</code> routine to resample the individual 2D spectra onto a common rectified pixel grid and combine the exposures for each slit with outlier rejection, using a threshold of 100.

2.4.1. Background Subtraction and Extraction

To correct the data for background light, we opted to use a full-MSA background solution, rather than a paired exposure differencing algorithm, for several reasons. First, subtracting a global background model maximizes the S/N in the final spectra by excluding the shot noise that would be added by using a low-S/N measure of the background from single adjoining shutters. Second, the CECILIA targets are extended objects with light from each galaxy contaminating the shutters above and below the primary shutter. As such, the typical background algorithms that directly subtract the detected signal above and below the primary shutter inevitably subtract some source light as well. This oversubtraction poses a particular issue at the wavelengths of bright emission lines, which frequently extend well beyond the typical 0."6 dither spacing of our observations in the background-subtracted 2D spectra. Finally, as described below, we found that a single global background model provided a good description of the background across the field, while also enabling useful checks on the systematics of our observations.

We constructed the global background model by combining data from all the illuminated shutters in the MSA. Each rectified and drizzled 2D science spectrum was masked to omit rows corresponding to continuum emission from target galaxies or from other sources identified in the slit. Pixels illuminated by extended emission lines were also masked. The full set of masked science spectra (including those from dedicated sky slitlets, which were not masked unless they included coincidental sources) were then median combined into a single 2D background model. The 2D background was averaged in the spectral direction in order to model the residual bar shadows that were not fully corrected by the calwebb_spec2 pipeline, and these residual bar shadows were then removed from the 2D background model. We then averaged the resulting 2D background model in the spatial direction, weighting each pixel by the number of spectra contributing to the 2D median at the corresponding point in order to construct a 1D average background model as a function of wavelength.

As a cross-check on the consistency of our global background model, we created similar models from subsets of the observed slits grouped by their position on the sky (quartiles in R.A. and decl.), on the MSA (quadrants 1, 2, 3, and 4), as well as by separating the portions of spectra falling on each detector (NRS1 and NRS2). The estimated 1D background was consistent across the field, but we found a small additive offset 19 between the NRS1 and NRS2 detectors. We therefore applied a compensatory offset to the portions of each slit's recorded background spectrum falling on NRS2 before

averaging the data from all slits to create the global background model.

Before subtracting the background from each 2D science spectrum, a slit-specific version of the global background mode was created that accounts for the NRS2 offset on the portions of that spectrum that fall on NRS2. This 1D model is then subtracted from each 2D science spectrum. Notably, the background model we derived is generally consistent with the predictions of the JWST Background Tool²⁰ (JBT) for our observations. However, a small additive offset is required to make the JBT prediction match the normalization of our empirical background model, and there are a number of small-scale spectral features in the empirical background that are unresolved or not included in the JBT spectrum.

Optimal extraction of the 1D spectra was performed using routines from msaexp. A spatial profile of the continuum emission for each background-subtracted 2D spectrum was created by averaging along the wavelength dimension after weighting by the pipeline-produced 2D weight mask and applying a sigma-clipping algorithm to mask contaminated pixels and bright emission lines. An analogous spatial profile of the nebular emission was also created for each source by averaging the 2D spectrum over small wavelength ranges centered at the locations of bright emission lines. Each resulting 1D spatial profile was then fit independently with a Gaussian model. The resulting fits were typically similar for the continuum and emission line profiles, with the median profile being 20% wider for the emission lines than the continuum. We used the Gaussian emission line spatial model to provide the weights for the optimal extraction, except in one case where the continuum profile was used owing to a visibly poor fit to the emission lines.

Despite the efforts described above, there are still unresolved issues in the data reduction resulting from known issues with JWST data products, ²¹ including uncertain variations in the spectral response as a function of slit position. Likewise, the unexplained additive offset between the NRS1 and NRS2 detectors, the residual bar shadows in the pipeline-processed 2D spectra, and the additive offset between our estimated background and the JBT predictions suggest that there are systematic effects (perhaps related to detector bias) that are incorrectly handled by the current pipeline tools and have uncertain downstream effects. While these uncertainties are not tolerable for the primary goal of CECILIA—precise abundance determinations of individual galaxies—we expect the stacking and normalization procedures described in Section 3 likely mitigate any systematic effects on our composite spectra.

3. The Characteristic Rest-optical Spectrum of $\langle z \rangle \sim$ 2.4 Galaxies

CECILIA contains some of the deepest spectra obtained during Cycle 1, with ~ 30 hr observations of individual galaxies using the NIRSpec/MSA and the G235M/F170LP configuration. These data offer a unique opportunity to investigate the spectra of high-z star-forming galaxies, revealing features that have long remained out of reach of ground-based observations. Given the uncertainties in the data reduction at the present time, we use composite spectra as a tool to investigate the nebular

¹⁹ The source of this offset is not clear, but we speculate that it stems from inconsistencies in the bias estimated from each detector.

 $^{{\}color{red}^{20}}\ https://jwst-docs.stsci.edu/jwst-other-tools/jwst-backgrounds-tool$

²¹ https://jwst-docs.stsci.edu/jwst-calibration-pipeline-caveats/known-issues-with-jwst-data-products

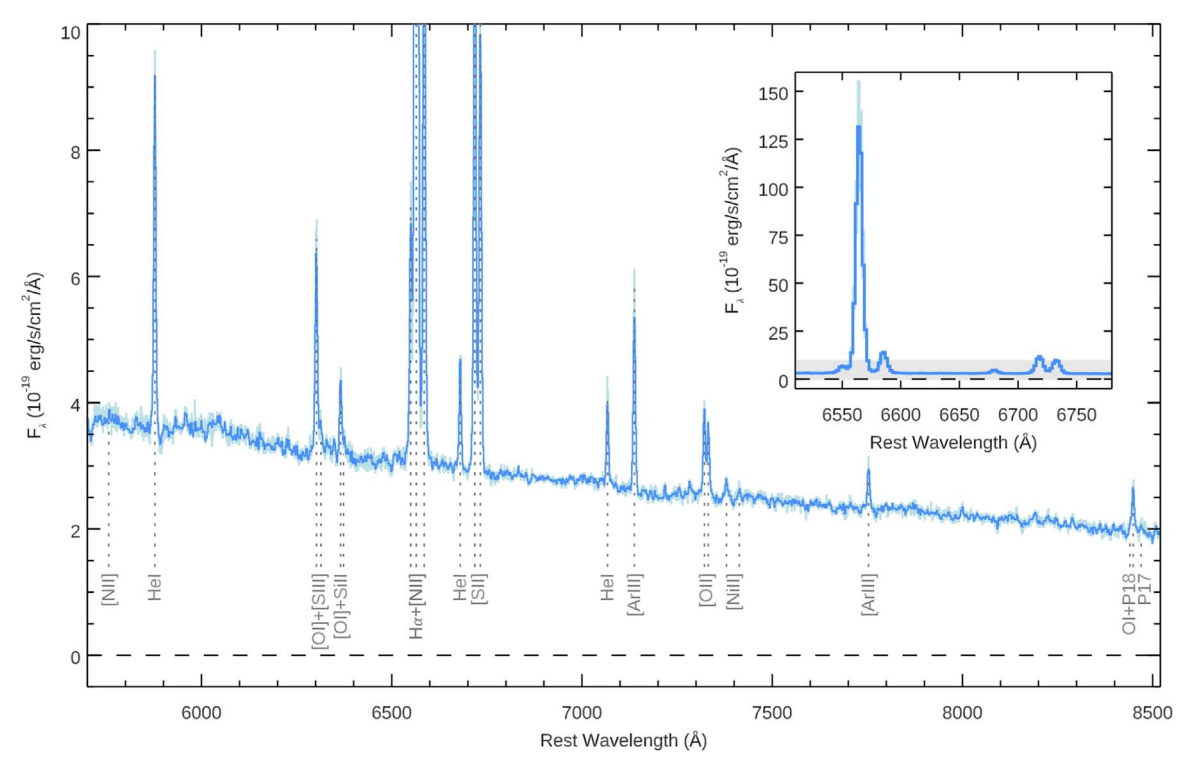


Figure 3. The median-combined composite spectrum for the CECILIA sample is shown by the medium blue line, where the individual galaxy spectra are scaled by the observed continuum at 6800-7000 Å before being combined. The stack is then rescaled so that the continuum in the same wavelength interval matches the median rest-frame continuum for the constituent galaxies. The 68% CI for the composite is indicated by the light blue shading, and detected emission lines of eight different elements (H, He, N, O, Si, S, Ar, and Ni) are identified by dotted gray lines. The inset panel shows a zoomed-out version of the composite, centered on $H\alpha$, [N II] $\lambda\lambda6550$, 6585, and [S II] $\lambda\lambda6718$, 6733, which are the only lines routinely observed in ground-based observations and shallower JWST spectra of individual high-z galaxies; the gray shaded region indicates the flux range shown in the full figure, where many fainter lines are visible.

emission lines observed in our data. We have two principal aims: (i) to illustrate the archetypal red rest-optical ($\lambda_{\rm rest} \approx 5700-8500$ Å) spectrum of a $z \sim 2$ galaxy, and (ii) to determine the typical range of emission line strengths. To achieve these goals, we construct two composite spectra, one including the stellar continuum and one only including the nebular emission. In this section, we describe how the two composite spectra are created, as well as their key features.

3.1. The Total Composite Spectrum

The flux scale of each reduced 1D spectrum is adjusted by comparing the observed continuum with the best-fit SED model of the same galaxy. This strategy has become common practice in analyzing JWST spectra of high-z galaxies as a way of accounting for uncertainties in the flux calibration. Specifically, we mask regions of the spectra with large deviations from the median flux level ($\ge 2 \times$ the median absolute deviation), which excludes not only strong emission lines but also any serious artifacts remaining in the data due to bad pixels and cosmic rays. We then use a low-order polynomial to define a multiplicative "slit loss" function for each object that forces the observed continuum to match the best-fit SED.

After this additional flux-correction step, the spectra are shifted into the rest frame and normalized by the median observed continuum flux in the region between $\lambda_{\rm rest} = 6800-7000\,\text{Å}$, where there are no emission lines; this portion of the spectrum is also approximately centered with respect to the auroral [S III] λ 6313 and [O II] $\lambda\lambda$ 7322, 7332 lines. The spectra are then interpolated onto a common rest-

frame wavelength array and median combined. The final stack is subsequently rescaled to match the median rest-frame continuum of all the constituent galaxies between $\lambda_{\rm rest} = 6800\text{--}7000\,\text{Å}$. Uncertainties are estimated by generating 1000 bootstrap-resampled composite spectra and calculating the 68% confidence interval (CI; analogous to asymmetric error bars) at each wavelength.

Figure 3 shows this composite spectrum (in medium blue) and the corresponding uncertainties (in light blue) over the range of rest-wavelengths with continuum S/N \gtrsim 15, where we define the S/N as the ratio of the composite spectrum to half the 68% CI. This requirement results in $\gtrsim\!75\%$ ($\geqslant\!17/23$ galaxies) contributing to the final composite at each wavelength. At the center of the wavelength range where the targeted auroral lines are found, the stack represents $\sim\!690$ object-hours of exposure time.

Aside from the "strong" $\text{H}\alpha$, [N II] $\lambda\lambda$ 6550, 6585, and [S II] $\lambda\lambda$ 6718, 6733 lines (highlighted in the inset panel in Figure 3), no other emission lines are routinely detected in ground-based spectra of individual $z\sim2$ galaxies. Lines longward of \sim 7000 Å are virtually inaccessible from the ground at $z\gtrsim2$, due to a combination of the rising thermal background in the K band and decreasing atmospheric transparency. In more recent studies of high-z galaxies using JWST/NIRSpec, emission lines in this wavelength range that are fainter than nebular [N II] and [S II] are only infrequently observed in individual galaxy spectra (e.g., Sanders et al. 2023b; Cameron et al. 2023; Shapley et al. 2023)—and even these relatively strong lines are not always visible in the spectra of some distant galaxies. In the composite spectrum shown in Figure 3, we identify emission lines from eight different elements (H, He, N, O, Si, S, Ar, and

Ni, denoted by the vertical dotted gray lines). Many of these have only rarely, if ever, been observed outside of the nearby Universe.

3.2. The Nebular Composite Spectrum

To quantify the strength of these emission lines, we construct a second, continuum-subtracted composite spectrum. In this case, after each spectrum is flux-corrected to match the best-fit SED, the model continuum is subtracted before the spectrum is shifted into the rest frame. To remove any remaining irregular wavelength-dependent errors in the continuum subtraction, we subtract a running median, using a large window $(\Delta \lambda_{\rm rest} \sim 200 \,\text{Å})$ to avoid overcorrecting near the emission lines. The spectra are then normalized by the measured flux in $H\alpha$ and median combined. Because $H\alpha$ falls in the detector gap for three galaxies, the nebular composite only includes 18 of the 23 galaxies used to construct the total composite spectrum. Finally, the resulting composite spectrum is converted to flux units (λF_{λ}) and rescaled so that the peak flux of (narrow) H α is 100. Figure 4 shows this composite spectrum (in medium blue), with the flux limit chosen to facilitate inspection of the semistrong and faint features. As before, uncertainties are estimated using bootstrapping (shown by the light blue shading). The same lines identified in Figure 3 are marked by dashed gray lines here.

We determine the typical strength of these emission lines by first fitting the median composite with a model containing 73 emission lines, drawn from the catalog reported by Esteban et al. (2004), who conducted a detailed analysis of Very Large Telescope (VLT) UVES (Dekker et al. 2000) echelle spectrophotometry of the Orion nebula. We select those lines in the wavelength range sampled by the CECILIA nebular composite that are measured to have a flux >0.01% of H α in the Esteban et al. (2004) spectrum. All of the lines are modeled as single Gaussians, have fixed relative wavelengths (i.e., the line centers are not allowed to move relative to one another), and are required to have the same width. For the strong [N II] $\lambda\lambda$ 6550, 6585 and semi-strong [O I] $\lambda\lambda$ 6302, 6365 doublets, which have relative strengths set by atomic physics, the ratios are fixed at 1:2.96 and 3.15:1, respectively (Froese Fischer & Saha 1983; Baluja & Zeippen 1988, 1988; Tachiev & Froese Fischer 2001). A second Gaussian is included to account for broad components under the strongest lines (H α , [N II] $\lambda\lambda$ 6550, 6585, and [SII] $\lambda\lambda$ 6718, 6733) and allowed to be offset in velocity relative to the narrow components of the same lines; all of the broad components are required to have the same line width and velocity offset. The addition of these components significantly improves the residuals from the model by accounting for excess flux detected near the $H\alpha + [NII]$ complex.

The 1000 bootstrap samples are fit using the same model, and the 68% highest density interval (HDI) for the distributions of measured fluxes are used to determine uncertainties on the reported line fluxes. Lines are considered well detected when they have a nonzero flux in >99% of fits and the maximum a posteriori (MAP) value for the line flux is $>3\sigma$. Nineteen emission lines satisfy these criteria and are listed in Table 1. We also include Si II λ 6373 (2.9 σ), the weaker [Ni II] line at 7414 Å (2.7 σ), the Paschen line at 8470 Å (3.1 σ , but only nonzero in 97.5% of the bootstrap stacks), and all of the broad components.

The dark blue curve in the top panels of Figure 4 represents the best-fit model containing the emission lines in Table 1, with the fit residuals shown by the medium blue line in the bottom panels. Recall that the peak of (narrow) $H\alpha$ is set to 100 in the nebular composite, so that the peak of the semi-strong and faint emission lines corresponds to their strengths relative to the narrow component of $H\alpha$. The MAP values are also reported in Table 1, along with the 68% HDI for each line. Because the uncertainties are calculated via bootstrap, note that these ranges reflect contributions from both observational uncertainties on the individual line measurements and physical variation among the objects in our sample.

4. Faint Emission Lines in High-redshift Star-forming Galaxies

In this section, we highlight individual semi-strong ($\approx 2\%$ –3% of H α) and faint ($\lesssim 1\%$ of H α) emission lines detected in the CECILIA composite spectra and briefly comment on how they may be used to study high-z galaxies.

4.1. Auroral Lines

Of all the faint lines present in the rest-optical spectra of star-forming regions, the auroral lines that can be used to implement the direct method of measuring metallicities have received the most attention in studies of high-z galaxies. Foremost among these is [O III] λ 4364, which falls at $\lambda_{\rm obs} \approx 1.3-1.7~\mu {\rm m}$ for the $z \sim 2-3$ CECILIA galaxies. As described in Section 2.2, CECILIA instead targets two auroral lines at longer wavelengths that are not only predicted to be stronger than [O III] λ 4364 but also fall at $\lambda_{\rm obs} \gtrsim 2.0~\mu {\rm m}$, where JWST is more sensitive. In total, three auroral lines fall in the wavelength range sampled by the composite spectra shown in Figures 3 and 4 and form the basis of our discussion here: [N II] λ 5756, [S III] λ 6313, and [O II] λ 7322, 7332.

The strongest of these is $[O II]\lambda\lambda7322$, 7332, with both lines observed to be $\sim 1\%$ the strength of the narrow component of H α (right panel of Figure 5). Sanders et al. (2023c) recently reported the detection of this feature (actually a quadruplet) in two z = 2.18 galaxies, which had each been observed for $\sim 15 \,\mathrm{hr}$ using Keck/MOSFIRE. Using their measurements to calculate direct-method oxygen abundances, they find moderate $12 + \log(O/H) = 7.89 \pm 0.20$ and $12 + \log(O/H) = 8.24 \pm 0.27$. Comparing these abundances to the predictions in the bottom panel of Figure 2, we see that they lie near the broad peak of the predicted line strengths and, thus, likely represent only the "tip of the iceberg": Other deep spectroscopic studies should uncover auroral [O II] lines in galaxies with a wider range of O/H. This is one of the main goals of the CECILIA program (Section 2.2), which includes many high-confidence detections of these lines in individual galaxy spectra that will be investigated in a subsequent paper.

The other auroral line specifically targeted by CECILIA is [S III] \(\lambda 6313 \) (middle panel of Figure 5), which samples a higher-ionization zone than auroral [O II]. Whereas this line is routinely used to measure abundances in nearby extragalactic H II regions, it has never been reported in observations of galaxies outside the local Universe. It is significantly detected in the CECILIA

 $^{^{22}}$ "Auroral" lines are forbidden transitions from the second (or higher) excited state of ions of heavy elements and can be paired with observations of the corresponding "nebular" lines (from the first excited state) to determine T_e in low-density gas where collisional de-excitation does not play a significant role.

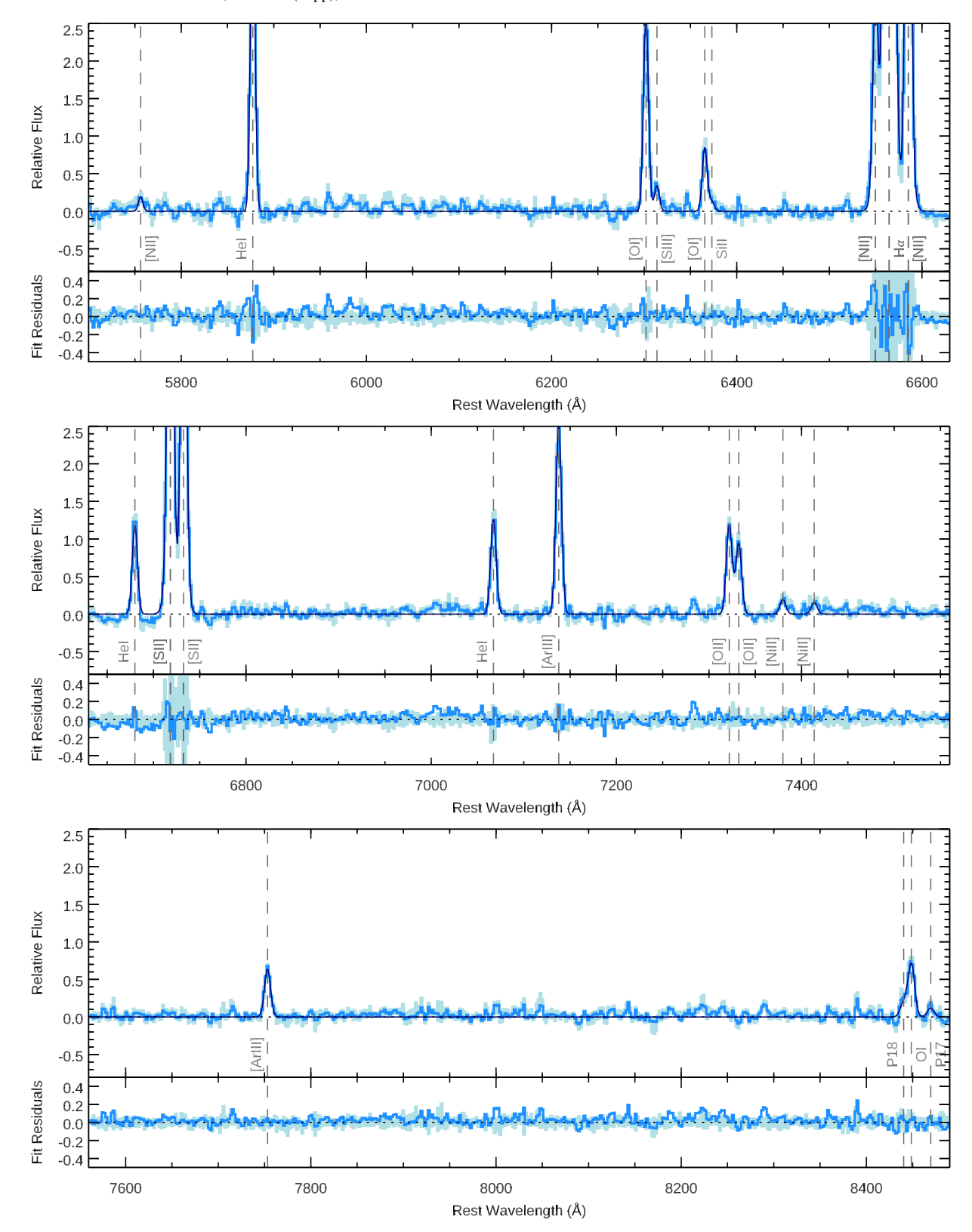


Figure 4. The nebular composite spectrum of the CECILIA sample is shown in medium blue, with the light blue shading representing the 68% CI determined via bootstrapping. The dark blue curve shows the best-fit model, which includes emission lines of eight different elements, identified by the dashed gray lines. The strengths of these lines relative to the narrow component of H α are reported in Table 1. The residuals from the model are shown in the bottom panels (medium blue), compared to the uncertainties on the median stack (light blue).

composites, and we have preliminary evidence of its presence in spectra of individual CECILIA galaxies. However, because of its faintness (0.29%–0.41% the strength of $H\alpha$) and proximity to the

comparatively stronger [O I] λ 6302 line, [S III] λ 6313 is unlikely to be accessible in shallower or lower-resolution JWST observations of objects similar to the CECILIA sample.

Table 1 Observed Line Fluxes Relative to $H\alpha$

Ion	$\lambda_{ m vac} \ (m A)$	$F(\lambda)$ (%)	Range (%)	Notes
	(71)	Narrow comp		
[N II]	5756.24	0.20	0.15-0.25	Auroral line
He I	5877.27	4.12	3.74-4.48	
[O I]	6302.04	2.80	2.36-3.08	
[S III]	6313.85	0.34	0.29-0.41	Auroral line
[O I]	6365.54	0.91	0.77 - 1.01	
Si II	6373.12	0.12	0.09-0.21	
[N II]	6549.86	2.55	1.86-3.02	
$H\alpha$	6564.62	100.00	•••	
[N II]	6585.27	7.59	5.54-8.99	
He I	6679.99	1.21	1.09-1.34	
[S II]	6718.29	7.33	5.55-7.76	
[S II]	6732.68	6.49	4.94-6.93	
He I	7067.23	1.25	1.07-1.51	
[Ar III]	7137.75	2.63	2.22-2.86	
[O II]	7321.94	1.21	1.10-1.38	Auroral line
[O II]	7332.21	0.95	0.88 - 1.12	Auroral line
[Ni II]	7379.86	0.22	0.15-0.30	
[Ni II]	7413.65	0.17	0.11-0.24	
[Ar III]	7753.23	0.64	0.57-0.72	
P18	8440.28	0.20	0.13-0.27	
OI	8448.57	0.73	0.64-0.87	
P17	8469.58	0.13	0.09-0.18	
		Broad compo	onents	
[N II]	6549.86	0.86	0.15-1.56	
$H\alpha$	6564.62	12.63	6.01-28.31	
[N II]	6585.27	2.55	0.45-4.65	
[S II]	6718.29	0.95	0.00-2.48	

Note. [F(H α_{narrow}) = 100].

6732.68

[SII]

The third auroral line observed in the composite spectra is $[N \text{ II}]\lambda 5756$, at 0.15%–0.25% the strength of $H\alpha$ (left panel of Figure 5). It is formally detected at 4.6σ in the stack but is likely too faint to be detected in the individual spectra of high-z galaxies, even using long exposure times with JWST. Still, for the sample of galaxies where it is possible to detect, it may serve as an important tool for calibrating the T_e relation between different ionization zones (e.g., Garnett 1992; Esteban et al. 2009; Croxall et al. 2016; Yates et al. 2020; Rogers et al. 2021).

0.81

0.00-1.50

We use our measurement of $[N II]\lambda 5756$ to calculate T_e and the corresponding direct-method ionic abundance. First, we use the line strengths for $[SII]\lambda\lambda6718$, 6733 to determine the electron density and find $n_e \approx 285$ cm⁻³, which is consistent with values previously reported for KBSS galaxies (Strom et al. 2017) and other $z \sim 2-3$ galaxy samples (e.g., Sanders et al. 2016). This density is then combined with the measurements of nebular and auroral [N II] to calculate T_e using the PyNeb package (Luridiana et al. 2015). However, because the nebular stack does not contain both H α and H β , which are required to determine the Balmer decrement and robustly constrain the reddening, we adopt the interquartile range in E(B-V) for the KBSS parent sample, E(B - V) = 0.06 - 0.47 (Strom et al. 2017). Using these values, we find $T_e[N \text{ II}] = 13,630 \pm 2540 \text{ K}$, where the reported uncertainties also capture the likely range in reddening for

 $z\sim 2-3$ galaxies. This temperature can be used to infer the abundances of low-ionization species, and we ultimately calculate $12+\log(\mathrm{N}^+/\mathrm{H}^+)=6.33^{+0.18}_{-0.30}$ and $12+\log(\mathrm{S}^+/\mathrm{H}^+)=5.70^{+0.16}_{-0.26}$ using the nebular lines for both ions; because the auroral $[\mathrm{O\,II}]\lambda\lambda7322$, 7332 lines are, by definition, strong functions of T_e , any $\mathrm{O}^+/\mathrm{H}^+$ abundance determined using $T_e[\mathrm{N\,II}]$ would have much larger uncertainties. We cannot confidently determine the contribution from other common (but unseen) ionization states of nitrogen and sulfur using the nebular composite alone and so do not report total abundances here, but we plan to revisit the issue of appropriate ionization correction factors for high-z galaxies in future work.

4.2. Other Semi-strong and Faint Lines

In addition to the three auroral emission lines, we also detect eight semi-strong and faint emission lines from four different heavy elements. Cutouts of the nebular composite spectrum near these features are shown in Figure 6, in the same manner as Figures 4 and 5.

The strongest of the lines is $[O I]\lambda 6302$ (upper-left panel of Figure 6), which is observed to be 2.36%–3.08% the strength of the narrow component of H α and is significantly stronger than the auroral [S III] λ 6313 line in its red wing. Its partner line at 6365 Å is $\approx 3.15 \times$ weaker as set by atomic physics and is blended with Si II λ 6373, which also probes mostly neutral and low-ionization gas. Rather than being an abundance diagnostic, $[O I]\lambda 6302$ is most commonly used as a way to identify the principal ionization mechanism in emission line galaxies using a form of the Baldwin-Philips-Terlevich diagram (Baldwin et al. 1981; Veilleux & Osterbrock 1987). It can also be useful for identifying contributions from diffuse ionized gas and shocks (e.g., Tüllmann & Dettmar 2000; Moy & Rocca-Volmerange 2002; Zhang et al. 2017). Although widely studied in the local Universe, including in large samples such as the Sloan Digital Sky Survey (Kewley et al. 2006; Law et al. 2021), $[OI]\lambda 6302$ is not commonly reported for individual $z \gtrsim 2$ galaxies. More recently, however, it has been observed in a handful of high-z galaxies with moderately deep ground-based or JWST spectroscopy (e.g., Sanders et al. 2023c; Cameron et al. 2023; Clarke et al. 2023). Given its typical strength, this semi-strong line should provide an accessible and promising method for discriminating between active galactic nuclei (AGNs) and star formation and probing low-ionization gas in high-z galaxies.

The lower-left panel of Figure 6 shows the widely spaced [Ar III] $\lambda\lambda$ 7138, 7753 lines, which, like lines of O⁺⁺, trace the gas in the high-ionization zone of star-forming regions. In lowz galaxies, the stronger [Ar III] λ 7138 line has been used to determine absolute argon abundances and relative abundance ratios, such as Ar/O (e.g., Berg et al. 2015; Croxall et al. 2016; Rogers et al. 2021), after accounting for unseen ionization states of Ar. At 2.22%–2.86% the strength of H α , comparable to $[O I]\lambda 6302$, this line is one of the strongest heavy metal lines present in the CECILIA nebular composite spectrum, aside from the familiar strong lines; Sanders et al. (2023c) find similar ratios for their two z = 2.18 galaxies. Thus, [Ar III] λ 7138 is also an attractive target for spectroscopic studies of galaxy enrichment. Although both Ar and O are nominally produced by the same mechanism in massive stars, differences in Ar/O as a function of overall enrichment could reflect a dependence of stellar nucleosynthesis on metallicity (e.g., Kennicutt et al. 2003; Izotov et al. 2006).

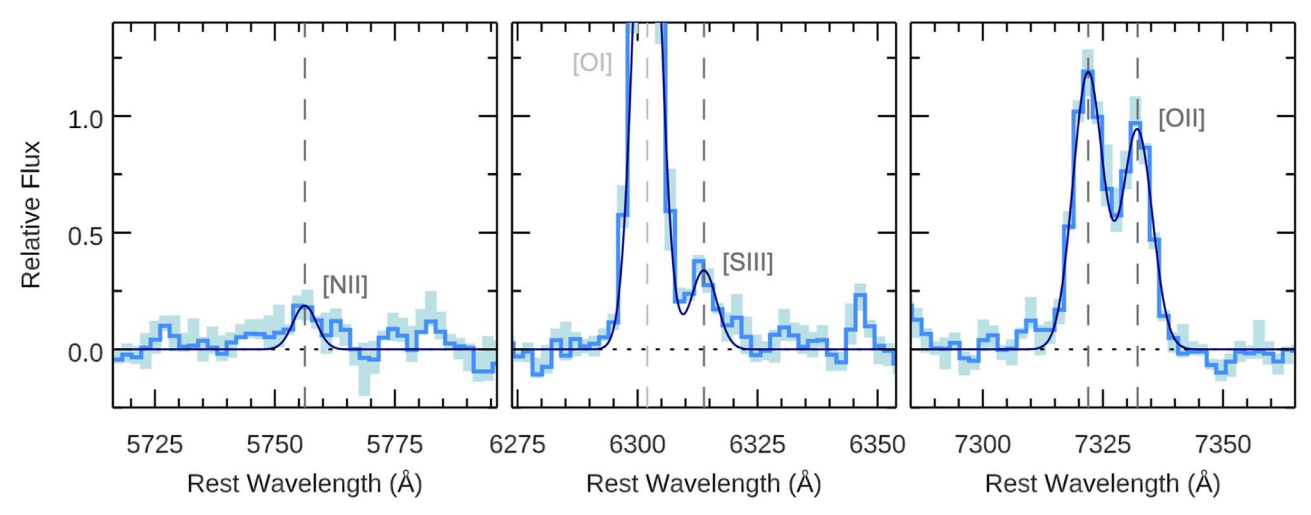


Figure 5. The three auroral lines observed in the CECILIA stack are shown in separate panels with the same flux scale, in the same manner as Figure 4. Auroral [N II] λ 5756 (left panel) is the weakest of the three and is estimated to be 0.15%–0.25% the strength of H α . Both [S III] λ 6313 (center panel) and [O II] λ 7322, 7332 (right panel) are noticeably stronger, and the oxygen lines are clearly the brightest auroral features in the $\lambda = 5700-8500$ Å range, with each being \sim 1% the strength of H α .

Permitted O_I at 8449 Å (upper-right panel of Figure 6) is one of the most commonly used recombination lines for measuring metallicity in astrophysical environments where such transitions can be observed (Maiolino & Mannucci 2019). Typically, however, metal recombination lines are too weak to be useful diagnostics, even in $z \sim 0$ galaxies and H II regions, so its presence in the CECILIA composite is unexpected. We consulted the database maintained by the Atomic Spectroscopy Data Center at the National Institute of Standards and Technology (NIST), but no other likely candidates for emission lines at the same rest wavelength were identified. O I λ 8449 is blended with the Paschen series line at 8440 Å (P18) in its left wing, and the neighboring Paschen line at 8470 Å (P17) is also detected in the nebular composite, relieving concerns that poor wavelength calibration may have led to misidentifying the line. The anomalous strength of this line in the Orion Nebula is in fact a longstanding puzzle (e.g., Morgan 1971; Danziger & Aaronson 1974), but Grandi (1975) showed that direct excitation by starlight is the most likely origin, rather than recombination from O^+ or Ly β fluorescence. The strength of O I $\lambda 8449$ in the CECILIA composite relative to H α (0.64%– 0.87%) is comparable to that reported for the Orion Nebula (0.56%; Esteban et al. 2004), suggesting that the same mechanism may also be dominant in high-z galaxies. If true, the contribution from direct excitation would severely limit the utility of O I λ 8449 as a metallicity tracer; García-Rojas et al. (2006) and García-Rojas et al. (2007) used both O I λ 7771 and O I λ 8449 to derive O⁺ abundances in Galactic H II regions but found an order-of-magnitude larger O^+/H^+ using $OI \lambda 8449$, likely due to this effect.

Also puzzling is the detection of [Ni II] $\lambda\lambda7380$, 7414 (shown in the lower-right panel of Figure 6), which are 0.15%–0.30% and 0.11%–0.24% the strength of H α , respectively. There are comparatively few references to the observation of this line in astrophysical objects, but a handful of studies have reported measurements of [Ni II] $\lambda7380$ and the corresponding Ni⁺ abundances in gaseous nebulae in the Milky Way (Dennefeld 1982; Fesen & Kirshner 1982; Henry & Fesen 1988; Esteban et al. 1999). In many of these cases, [Ni II] $\lambda7380$ was seen to be much stronger than expected relative to the associated [Ni II] $\lambda7414$ line, which is only marginally detected in the CECILIA composite spectra. Other authors have explained this

by invoking fluorescence by the UV continuum, similar to [Fe II] lines (Lucy 1995) and/or collisional excitation in very high density ($n_e \approx 10^6 \text{ cm}^{-3}$) gas (Bautista et al. 1996). Similar to O I λ 8449, no reasonable alternatives were identified in the NIST database, but without significantly detecting [Fe II] lines that may also be impacted by the same physical mechanism, it is difficult to speculate about its appearance here.

4.3. Broad $H\alpha$

Broad line emission has been observed in both spectra of individual galaxies and composite spectra of galaxies at $z\sim 2$ and is usually attributed to galaxy-scale ionized gas outflows (see Section 4.6 of the review by Förster Schreiber & Wuyts 2020, and references therein); in contrast, the frequently brighter, narrow components of emission lines trace galaxies' star-forming regions. Both AGNs (e.g., Nesvadba et al. 2008; Förster Schreiber et al. 2014; Genzel et al. 2014; Cresci et al. 2015) and star formation (e.g., Genzel et al. 2011; Davies et al. 2019; Freeman et al. 2019) can generate these outflows, resulting in differences in inferred outflow velocity (i.e., emission line width), with AGNs typically driving higher-velocity outflows than feedback from massive stars.

In order to achieve a good fit to the nebular composite spectrum, we include two Gaussian components for the strongest lines to account for excess flux that results in large residuals from a model with only a single (narrow) component. Based on the results from fitting the 1000 bootstrap samples, these broad components have a FWHM of 536^{+45}_{-167} km s⁻¹ and are consistent with no velocity offset relative to the narrow components, which have a FWHM of 288^{+15}_{-20} km s⁻¹. The broad H α line is 6.01%–28.31% the strength of the narrow component of $H\alpha$, with significantly weaker broad components observed for nebular [N II] and [S II]; this is consistent with the low end of the range reported for a similar sample of $z \sim 2$ starforming galaxies (Freeman et al. 2019). If these components in the CECILIA composite do indeed reflect the presence of ionized gas outflows, the evidence for broad (albeit weak) line emission in forbidden transitions and the moderate velocity width suggest that they are likely driven by star formation. Comparable FWHM velocities of $\sim 400-500 \text{ km s}^{-1}$ are observed in deep VLT/SINFONI (Eisenhauer et al. 2003;

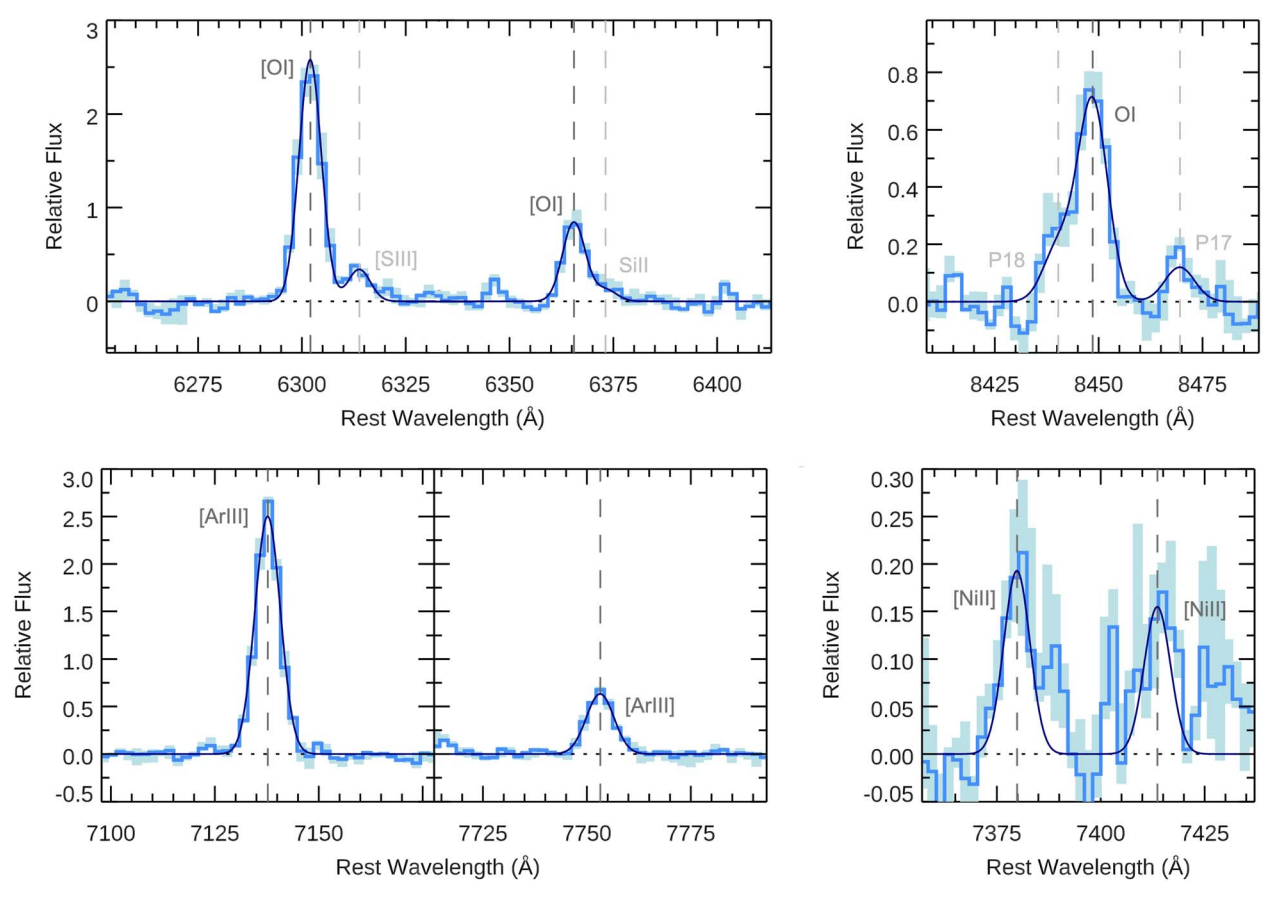


Figure 6. Semi-strong and faint emission lines of four elements—O, Si, Ar, and Ni—are shown in the same manner as Figures 4 and 5, but with a different flux range used each panel. The top row shows forbidden [O I] λ 6302, 6565 (upper left), with [S III] λ 6313 and Si II λ 6373 in the red wings of each line, respectively, and permitted O I at 8449 Å, blended with Pa18 (upper right). The bottom row shows forbidden lines of [Ar III] λ 7138, 7753 (lower left) and [Ni II] λ 7380, 7414 (lower right). The stronger [O I] and [Ar III] lines have now been observed in deep spectra of individual high-z galaxies (e.g., Sanders et al. 2023c; Cameron et al. 2023), but the permitted O I λ 8449 line and forbidden [Ni II] are only rarely observed, even in observations of nearby galaxies and H II regions.

Bonnet et al. 2004) spectra of star-forming clumps at $z \sim 2$ (e.g., Newman et al. 2012; Förster Schreiber et al. 2019). However, because of the additional median filtering required to remove remaining fluctuations in the continuum of individual galaxy spectra (Section 3.2), the detailed properties of any broad line emission in the CECILIA stack could be systematically biased.

5. Conclusions

We have reported the first results from the CECILIA program (JWST PID 2593), which obtained ultra-deep $\sim\!\!30\,\mathrm{hr}$ NIRSpec/G235M observations of 33 star-forming galaxies at $z\sim 1{\text -}3$. Using data for 23 of these galaxies, we constructed rest-optical composite spectra, both with and without the stellar continuum, corresponding to exposure times of 690 object-hours and 540 object-hours, respectively. These composites, shown in Figures 3 and 4, provide one of the most detailed views to date of star-forming galaxies in the early Universe and function as an atlas of their characteristic rest-optical emission line spectra.

The principal findings based on our analysis of the stacked spectra are as follows:

1. We significantly detect emission lines of eight different elements (H, He, N, O, Si, S, Ar, and Ni), including evidence for broad line emission under H α , [N II] $\lambda\lambda6550$, 6585, and [S II] $\lambda\lambda6718$, 6733. The strengths

- of these lines relative to the narrow component of $H\alpha$ are reported in Table 1.
- 2. Aside from strong [N II], H α , and [S II], which have previously been studied in large ground-based spectroscopic samples, the majority of emission lines are $\lesssim 3\%$ the strength of H α . Some of these features, such as [O I] $\lambda 6302$ (shown in the upper-left panel of Figure 6), are now being detected in JWST spectra of individual high-z galaxies, and we expect other lines with strengths $\gtrsim 2\%$ –3% that of H α to be good candidates for spectroscopic follow-up of large samples. In addition to the stronger forbidden [O I] line, these semi-strong lines include the He I line at $\lambda 5877$ and [Ar III] $\lambda 7138$ (shown in the bottom-left panel of Figure 6).
- 3. The three auroral emission lines present at $\lambda_{\rm rest} \approx 5700-8500$ ([N II] $\lambda 5756$, [S III] $\lambda 6313$, and [O II] $\lambda \lambda 7322$, 7332, shown in Figure 5) are $\lesssim 1\%$ the strength of H α . Using our measurements of auroral and nebular [N II], we find T_e [N II] = $13,630 \pm 2540$ K, which is the first time a T_e has been reported for high-redshift galaxies using this tracer. Although we have not reported the significance of detections in individual galaxy spectra in this work, it seems likely that these auroral lines will remain out of reach of typical observations of high-z galaxies, particularly those with low SFRs, low ionization, and/or high metallicity. This only underscores the need for more accurate line-ratio diagnostics for

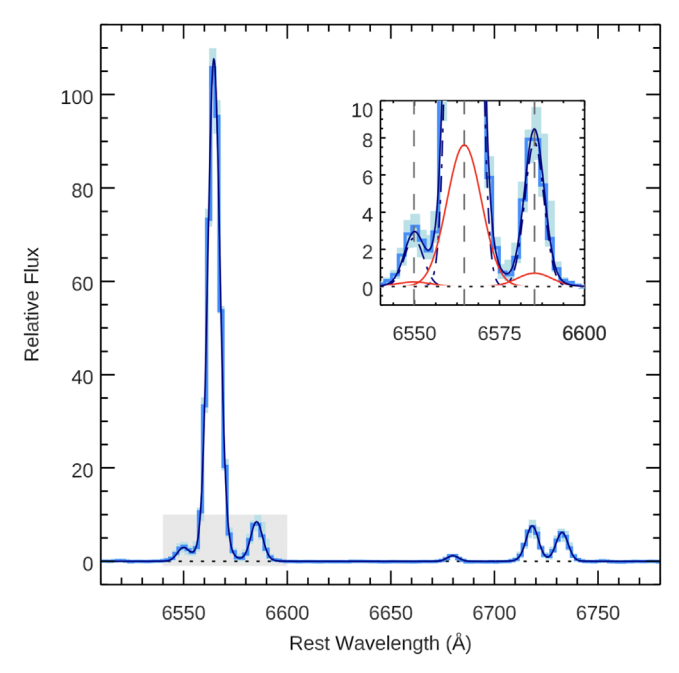


Figure 7. The same nebular composite spectrum from Figure 4 is shown near the strong H α , [N II] $\lambda\lambda$ 6550, 6585, and [S II] $\lambda\lambda$ 6718, 6733 lines, with a more extended flux range to show the peaks of the lines. The inset panel is a zoom-in on the gray shaded region, highlighting the broad components of H α and [N II] (in red). The narrow components of all three lines are illustrated by the dotteddashed navy curves.

- metallicity that make use of the strong and semi-strong
- emission lines present in galaxies' rest-optical spectra. 4. We measure broad $(536^{+45}_{-167}~{\rm km~s^{-1}}~{\rm FWHM})$ line emission under the strongest lines and a broad component of H α that is 6.01%–28.31% the strength of the narrow component (Figure 7). These results appear indicative of star-formation-driven outflows. However, we caution that, owing to remaining uncertainties in the flux calibration (see the discussion in Section 2.4), the appearance of this component should not be overinterpreted. We defer a more detailed discussion of broad line emission and its connection to galaxy outflows to a future paper.

JWST is delivering on its promise to provide access to faint emission lines in the spectra of ≥ 2 galaxies, evidenced not only by what we have presented in this Letter, but also by the many exciting results based on NIRSpec/MSA and NIRCam grism spectroscopy that have been published over the last year. Deep observations, such as those obtained as part of CECILIA and outlined here, will be critical for developing and testing the new tools necessary to accurately interpret this wealth of data. As known issues with JWST data products continue to be resolved, it will benefit the extragalactic community to revisit some of the earliest observations—with the benefit of hindsight and these new tools—in order to maximize the scientific impact of these data. To aid in this effort, forthcoming work with CECILIA will focus on (i) T_e measurements and direct-method metallicities for the sample of galaxies introduced here, as well as (ii) new line-ratio diagnostics for gas-phase oxygen abundance.

Acknowledgments

The authors thank Jane Rigby, Taylor Hutchison, and Marcia Rieke for their advice regarding the reduction of the JWST data, as well as Jenny Greene for her input on the scope of the discussion. We are also grateful to the JWST/NIRSpec team for their ongoing work to support this complex and powerful instrument.

A.L.S., G.C.R., and R.F.T. acknowledge partial support from the JWST-GO-02593.008-A, JWST-GO-02593.004-A, and JWST-GO-02593.006-A grants, respectively. R.F.T. also acknowledges support from the Pittsburgh Foundation (grant ID UN2021-121482) and the Research Corporation for Scientific Advancement (Cottrell Scholar Award, grant ID

This work is primarily based on observations made with NASA/ESA/CSA JWST, associated with PID 2593, which can be accessed via doi:10.17909/x66z-p144. The data were obtained from the Mikulski Archive for Space Telescopes (MAST) at the Space Telescope Science Institute, which is operated by the Association of Universities for Research in Astronomy, Inc., under NASA contract NAS 5-03127 for JWST.

Some of the data used to generate the original line flux predictions were obtained at the W.M. Keck Observatory, which is operated as a scientific partnership between the California Institute of Technology, the University of California, and NASA. The Observatory was made possible by the generous financial support of the W.M. Keck Foundation, and the authors wish to recognize and acknowledge the significant cultural role and reverence that the summit of Maunakea has within the indigenous Hawaiian community.

Facility: JWST (NIRSpec).

Software: BPASSv2 (Stanway et al. 2016; Eldridge et al. 2017), Cloudy (Ferland et al. 2013), GalDNA (Strom et al. 2018), JWST Calibration Pipeline (Bushouse et al. 2023), grizli (Brammer 2023), msaexp (Brammer 2022), PyNeb (Luridiana et al. 2015).

ORCID iDs

Allison L. Strom https://orcid.org/0000-0001-6369-1636 Gwen C. Rudie https://orcid.org/0000-0002-8459-5413 Ryan F. Trainor https://orcid.org/0000-0002-6967-7322 Gabriel B. Brammer https://orcid.org/0000-0003-2680-005X

Michael V. Maseda https://orcid.org/0000-0003-0695-4414 Menelaos Raptis https://orcid.org/0009-0008-2226-5241 Noah S. J. Rogers https://orcid.org/0000-0002-0361-8223 Charles C. Steidel https://orcid.org/0000-0002-4834-7260 Yuguang Chen (陈昱光) forcid.org/0000-0003-4520-5395

David R. Law https://orcid.org/0000-0002-9402-186X

References

Arellano-Córdova, K. Z., Berg, D. A., Chisholm, J., et al. 2022, ApJL, 940. L23 Baldwin, J. A., Phillips, M. M., & Terlevich, R. 1981, PASP, 93, 5 Baluja, K. L., & Zeippen, C. J. 1988, JPhB, 21, 1455 Bautista, M. A., Peng, J., & Pradhan, A. K. 1996, ApJ, 460, 372 Belfiore, F., Maiolino, R., Bundy, K., et al. 2015, MNRAS, 449, 867 Berg, D. A., Skillman, E. D., Croxall, K. V., et al. 2015, ApJ, 806, 16 Bonnet, H., Conzelmann, R., Delabre, B., et al. 2004, Proc. SPIE, 5490, 130

```
Brammer, G. 2022, msaexp: NIRSpec analysis tools, v0.3.4, Zenodo, doi:10.
   5281/zenodo.7299500
Brammer, G. 2023, grizli, v1.8.2, Zenodo, doi:10.5281/zenodo.7712834
Brinchmann, J. 2023, MNRAS, 525, 2087
Brinchmann, J., Charlot, S., White, S. D. M., et al. 2004, MNRAS, 351, 1151
Bushouse, H., Eisenhamer, J., Dencheva, N., et al. 2023, JWST Calibration
   Pipeline, v1.11.0, Zenodo, doi:10.5281/zenodo.8067394
Cameron, A. J., Saxena, A., Bunker, A. J., et al. 2023, A&A, 677, A115
Chabrier, G. 2003, PASP, 115, 763
Christensen, L., Laursen, P., Richard, J., et al. 2012, MNRAS, 427, 1973
Clarke, L., Shapley, A., Sanders, R. L., et al. 2023, ApJ, 957, 81
Cresci, G., Mainieri, V., Brusa, M., et al. 2015, ApJ, 799, 82
Croxall, K. V., Pogge, R. W., Berg, D. A., Skillman, E. D., & Moustakas, J.
   2016, ApJ, 830, 4
Curti, M., D'Eugenio, F., Carniani, S., et al. 2023, MNRAS, 518, 425
Danziger, I. J., & Aaronson, M. 1974, PASP, 86, 208
Davies, R. L., Förster Schreiber, N. M., Übler, H., et al. 2019, ApJ, 873, 122
Dekker, H., D'Odorico, S., Kaufer, A., Delabre, B., & Kotzlowski, H. 2000,
   Proc. SPIE, 4008, 534
Dennefeld, M. 1982, A&A, 112, 215
Eisenhauer, F., Abuter, R., Bickert, K., et al. 2003, Proc. SPIE, 4841, 1548
Eldridge, J. J., Stanway, E. R., Xiao, L., et al. 2017, PASA, 34, e058
Esteban, C., Bresolin, F., Peimbert, M., et al. 2009, ApJ, 700, 654
Esteban, C., Peimbert, M., García-Rojas, J., et al. 2004, MNRAS, 355, 229
Esteban, C., Peimbert, M., Torres-Peimbert, S., García-Rojas, J., &
   Rodríguez, M. 1999, ApJS, 120, 113
Ferland, G. J., Porter, R. L., van Hoof, P. A. M., et al. 2013, RMxAA, 49, 137
Fesen, R. A., & Kirshner, R. P. 1982, ApJ, 258, 1
Förster Schreiber, N. M., Genzel, R., Newman, S. F., et al. 2014, ApJ, 787, 38
Förster Schreiber, N. M., Übler, H., Davies, R. L., et al. 2019, ApJ, 875, 21
Förster Schreiber, N. M., & Wuyts, S. 2020, ARA&A, 58, 661
Freeman, W. R., Siana, B., Kriek, M., et al. 2019, ApJ, 873, 102
Froese Fischer, C. F., & Saha, H. P. 1983, PhRvA, 28, 3169
García-Rojas, J., Esteban, C., Peimbert, A., et al. 2007, RMxAA, 43, 3
García-Rojas, J., Esteban, C., Peimbert, M., et al. 2006, MNRAS, 368, 253
Garnett, D. R. 1992, AJ, 103, 1330
Genzel, R., Förster Schreiber, N. M., Rosario, D., et al. 2014, ApJ, 796, 7
Genzel, R., Newman, S., Jones, T., et al. 2011, ApJ, 733, 101
Grandi, S. A. 1975, ApJ, 196, 465
Henry, R. B. C., & Fesen, R. A. 1988, ApJ, 329, 693
Izotov, Y. I., Stasińska, G., Meynet, G., Guseva, N. G., & Thuan, T. X. 2006,
   A&A, 448, 955
James, B. L., Pettini, M., Christensen, L., et al. 2014, MNRAS, 440, 1794
Kashino, D., Lilly, S. J., Matthee, J., et al. 2023, ApJ, 950, 66
Katz, H., Saxena, A., Cameron, A. J., et al. 2023, MNRAS, 518, 592
Kauffmann, G., Heckman, T. M., Tremonti, C., et al. 2003, MNRAS,
   346, 1055
Kennicutt, R. C., Jr, Bresolin, F., & Garnett, D. R. 2003, ApJ, 591, 801
Kewley, L. J., Groves, B., Kauffmann, G., & Heckman, T. 2006, MNRAS,
  372, 961
Kewley, L. J., Nicholls, D. C., & Sutherland, R. S. 2019, ARA&A, 57, 511
Kocevski, D. D., Onoue, M., Inayoshi, K., et al. 2023, ApJL, 954, L4
Laseter, I. H., Maseda, M. V., Curti, M., et al. 2023, arXiv:2306.03120
Law, D. R., Ji, X., Belfiore, F., et al. 2021, ApJ, 915, 35
Law, D. R., Steidel, C. C., Shapley, A. E., et al. 2012, ApJ, 745, 85
Lucy, L. B. 1995, A&A, 294, 555
Luridiana, V., Morisset, C., & Shaw, R. A. 2015, A&A, 573, A42
Maiolino, R., & Mannucci, F. 2019, A&ARv, 27, 3
```

Masters, D., McCarthy, P., Siana, B., et al. 2014, ApJ, 785, 153

```
McLean, I. S., Steidel, C. C., Epps, H., et al. 2010, Proc. SPIE, 7735, 77351E
McLean, I. S., Steidel, C. C., Epps, H. W., et al. 2012, Proc. SPIE, 8446,
  84460I
Mingozzi, M., Belfiore, F., Cresci, G., et al. 2020, A&A, 636, A42
Morgan, L. A. 1971, MNRAS, 153, 393
Moy, E., & Rocca-Volmerange, B. 2002, A&A, 383, 46
Nesvadba, N. P. H., Lehnert, M. D., De Breuck, C., Gilbert, A. M., &
  van Breugel, W. 2008, A&A, 491, 407
Newman, S. F., Shapiro Griffin, K., Genzel, R., et al. 2012, ApJ, 752, 111
Oesch, P. A., Brammer, G., Naidu, R. P., et al. 2023, MNRAS, 525, 2864
Pontoppidan, K. M., Barrientes, J., Blome, C., et al. 2022, ApJL, 936, L14
Rauscher, B. J. 2023, arXiv:2306.03250
Rhoads, J. E., Wold, I. G. B., Harish, S., et al. 2023, ApJL, 942, L14
Rogers, N. S. J., Skillman, E. D., Pogge, R. W., et al. 2021, ApJ, 915, 21
Rudie, G. C., Steidel, C. C., Trainor, R. F., et al. 2012, ApJ, 750, 67
Sanders, R. L., Shapley, A. E., Clarke, L., et al. 2023c, ApJ, 943, 75
Sanders, R. L., Shapley, A. E., Kriek, M., et al. 2015, ApJ, 799, 138
Sanders, R. L., Shapley, A. E., Kriek, M., et al. 2016, ApJ, 816, 23
Sanders, R. L., Shapley, A. E., Reddy, N. A., et al. 2020, MNRAS, 491, 1427
Sanders, R. L., Shapley, A. E., Topping, M. W., Reddy, N. A., &
  Brammer, G. B. 2023a, arXiv:2303.08149
Sanders, R. L., Shapley, A. E., Topping, M. W., Reddy, N. A., &
  Brammer, G. B. 2023b, ApJ, 955, 54
Schaerer, D., Marques-Chaves, R., Barrufet, L., et al. 2022, A&A, 665, L4
Shapley, A. E., Reddy, N. A., Kriek, M., et al. 2015, ApJ, 801, 88
Shapley, A. E., Reddy, N. A., Sanders, R. L., Topping, M. W., &
  Brammer, G. B. 2023, ApJL, 950, L1
Sharples, R., Bender, R., Agudo Berbel, A., et al. 2013, Msngr, 151, 21
Simcoe, R. A., Burgasser, A. J., Bernstein, R. A., et al. 2008, Proc. SPIE, 7014,
  70140U
Simcoe, R. A., Burgasser, A. J., Bochanski, J. J., et al. 2010, Proc. SPIE, 7735,
Stanway, E. R., Eldridge, J. J., & Becker, G. D. 2016, MNRAS, 456, 485
Steidel, C. C., Erb, D. K., Shapley, A. E., et al. 2010, ApJ, 717, 289
Steidel, C. C., Rudie, G. C., Strom, A. L., et al. 2014, ApJ, 795, 165
Steidel, C. C., Strom, A. L., Pettini, M., et al. 2016, ApJ, 826, 159
Strom, A. L., Rudie, G. C., Chen, Y., et al. 2021, CECILIA: A direct-method
  metallicity calibration for Cosmic Noon through the Epoch of Reionization,
  JWST Proposal. Cycle 1, ID, #2593
Strom, A. L., Steidel, C. C., Rudie, G. C., et al. 2017, ApJ, 836, 164
Strom, A. L., Steidel, C. C., Rudie, G. C., Trainor, R. F., & Pettini, M. 2018,
   ApJ, 868, 117
Sun, F., Egami, E., Pirzkal, N., et al. 2023, ApJ, 953, 53
Tachiev, G., & Froese Fischer, C. 2001, CaJPh, 79, 955
Taylor, A. J., Barger, A. J., & Cowie, L. L. 2022, ApJL, 939, L3
Topping, M. W., Shapley, A. E., Reddy, N. A., et al. 2020, MNRAS, 499, 1652
Trainor, R. F., Steidel, C. C., Strom, A. L., & Rudie, G. C. 2015, ApJ, 809, 89
Trainor, R. F., Strom, A. L., Steidel, C. C., & Rudie, G. C. 2016, ApJ, 832, 171
Tremonti, C. A., Heckman, T. M., Kauffmann, G., et al. 2004, ApJ, 613, 898
Trump, J. R., Arrabal Haro, P., Simons, R. C., et al. 2023, ApJ, 945, 35
Trussler, J. A. A., Adams, N. J., Conselice, C. J., et al. 2023, MNRAS,
  523, 3423
Tüllmann, R., & Dettmar, R. J. 2000, A&A, 362, 119
Veilleux, S., & Osterbrock, D. E. 1987, ApJS, 63, 295
Wisnioski, E., Förster Schreiber, N. M., Wuyts, S., et al. 2015, ApJ, 799,
  209
Yates, R. M., Schady, P., Chen, T. W., Schweyer, T., & Wiseman, P. 2020,
   A&A, 634, A107
Zhang, K., Yan, R., Bundy, K., et al. 2017, MNRAS, 466, 3217
```